

Stellar Bars in Isolated Gas-Rich Spiral Galaxies Do Not Slow Down

Angus Beane,¹★ Lars Hernquist,¹ Elena D’Onghia,^{2,3} Federico Marinacci,⁴ Charlie Conroy,¹ Jia Qi,⁵
 Laura V. Sales,⁶ Paul Torrey,⁵ Mark Vogelsberger⁷

¹*Center for Astrophysics | Harvard & Smithsonian, Cambridge, MA, USA*

²*Department of Physics, University of Wisconsin-Madison, Madison, WI, USA*

³*Department of Astronomy, University of Wisconsin-Madison, Madison, WI, USA*

⁴*Department of Physics & Astronomy ‘Augusto Righi’, University of Bologna, Bologna, Italy*

⁵*Department of Astronomy, University of Florida, Gainesville, FL, USA*

⁶*Department of Physics & Astronomy, University of California, Riverside, CA, USA*

⁷*Department of Physics, Massachusetts Institute of Technology, Cambridge, MA, USA*

Accepted XXX. Received YYY; in original form ZZZ

ABSTRACT

Elongated bar-like features are ubiquitous in galaxies, occurring at the centers of approximately two-thirds of spiral disks. Due to gravitational interactions between the bar and the other components of galaxies, it is expected that angular momentum and matter will redistribute over long (Gyr) timescales in barred galaxies. Previous work ignoring the gas phase of galaxies has conclusively demonstrated that bars should slow their rotation over time due to their interaction with dark matter halos. We have performed a simulation of a Milky Way-like galactic disk hosting a strong bar which includes a state-of-the-art model of the interstellar medium and a live dark matter halo. In this simulation the bar pattern does not slow down over time, and instead remains at a stable, constant rate of rotation. This behavior has been observed in previous simulations using more simplified models for the interstellar gas but it has remained unexplained. We propose that the gas phase of the disk and the dark matter halo act in concert to stabilize the bar pattern speed and prevent the bar from slowing down or speeding up. We find that in a Milky Way-like disk, a gas fraction of only about 5% is necessary for this mechanism to operate. This result naturally explains why nearly all observed bars rotate rapidly and is especially relevant for our understanding of how the Milky Way arrived at its present state.

Key words: galaxies: bar - galaxies: disc - galaxies: evolution - galaxies: kinematics and dynamics

1 INTRODUCTION

244.0pt

508.0pt

Approximately two-thirds of spiral disks host an elongated bar-like feature at their center (Eskridge et al. 2000; Menéndez-Delmestre et al. 2007), including our own Milky Way (Johnson 1957; Blitz & Spergel 1991). The ubiquity of bars is not difficult to explain, since stellar disks simulated in isolation almost always form bar-like structures (Hohl 1971). Several studies have shown that a spherical potential, such as a stellar bulge or dark matter halo, acts to stabilize a stellar disk against the bar instability (Ostriker & Peebles 1973; Hohl 1976).

It is more difficult to reconcile numerical simulations with the observed pattern speeds of extragalactic bars. Currently, the best technique for measuring the pattern speeds of individual galaxies is the Tremaine-Weinberg method (Tremaine & Weinberg 1984b; Corsini 2011). This method has recently been applied to samples of galaxies from the MaNGA survey (Guo et al. 2019; Garma-Oehmichen et al. 2020). These recent studies confirm what was found in earlier studies

– that nearly all extragalactic bars are fast rotators (i.e., they rotate close to their maximum rotation rate)

This is a problem for theoretical simulations, for which there is ample evidence that galactic bars should resonantly interact with the dark matter halo, causing the bar to slow down over time (Hernquist & Weinberg 1992; Debattista & Sellwood 2000; Athanassoula & Misiriotis 2002; Athanassoula 2002, 2003; O’Neill & Dubinski 2003; Holley-Bockelmann et al. 2005; Martinez-Valpuesta et al. 2006; Weinberg & Katz 2007; Dubinski et al. 2009). The physical mechanism of this interaction can be understood as an angular form of dynamical friction between the bar and the dark matter halo. While studied in detail for the bar (Tremaine & Weinberg 1984a; Weinberg 1985), this process is generic for any non-axisymmetric disturbance (Lynden-Bell & Kalnajs 1972). For an old but still useful review of bar dynamics, see Sellwood & Wilkinson (1993)

Bar pattern speeds are usually measured using the parameter $\mathcal{R} = R_{\text{CR}}/R_{\text{b}}$, where R_{CR} is the corotation radius and R_{b} is the bar length.¹

¹ The radius of corotation R_{CR} is defined for circular orbits as the radius at which the orbital frequency is equal to the pattern speed, Ω_{p} , of a given non-axisymmetric feature. In a galaxy with a constant circular velocity V_{c} , it is given by $R_{\text{CR}} = V_{\text{c}}/\Omega_{\text{p}}$.

★ E-mail: angus.beane@cfa.harvard.edu (AB)

Galaxies with $\mathcal{R} < 1.4$ are considered “fast rotators” while galaxies with $\mathcal{R} > 1.4$ are considered “slow rotators” (Debattista & Sellwood 2000). Galaxies with $\mathcal{R} < 1$ are not thought to be stable (Contopoulos 1980). Observational estimates of the pattern speeds of bars indicate that nearly all galaxies have $1 < \mathcal{R} < 1.4$ (Corsini 2011; Aguerri et al. 2015; Guo et al. 2019; Garma-Oehmichen et al. 2020).

While the interaction between the bar and a dark matter halo is well-understood theoretically, this is not the case for the interaction between a bar and a gaseous disk. Some argue that the gas disk should slow down the bar more (Athanasoula 2003), while others argue that the tendency of the bar to drive gas inwards means the bar should speed up due to the effect of the gas disk (Athanasoula et al. 2013; Athanasoula 2014). Since the gas phase typically only contributes about 10–20% of the mass of a galaxy at the present day, one might naively expect it to have a subdominant effect on the bar. However, because gas is collisional, it can participate in non-resonant angular momentum exchange with the bar (Hopkins & Quataert 2011). Thus, numerical work has shown that the gas phase can have a stronger influence on a bar than its contribution to the mass of a galaxy would suggest (Villa-Vargas et al. 2010; Athanasoula et al. 2013).

We have performed a simulation of a disk galaxy using the finite-volume, gravito-hydrodynamics code AREPO (Springel 2010). We use the galaxy formation model Stars and Multiphase Gas in GaLaxiEs (SMUGGLE; Marinacci et al. 2019). This disk galaxy exhibits almost no evolution in the bar pattern speed over several Gyr when the gas phase is accounted for and properly modeled. This behavior has been observed in a few previous works (Friedli & Benz 1993; Villa-Vargas et al. 2010; Athanasoula 2014). However, we are the first to exhibit that the behavior ought to be present in a large fraction of galaxies, since it occurs in our simulation with gas fractions as low as about 5%. We are also the first to provide a physical explanation of the behavior with clear observational predictions.

We show synthetic *Hubble Space Telescope* images of our barred galaxy in a case with and without gas in Fig. 1. We see that the bar grows longer and stronger without gas, while it remains at approximately the same length and strength when gas is included. Details on the production of these synthetic images are given in Appendix C.

In Section 2, we describe our initial setup, numerical model, and details on our bar analysis procedures. In Section 3, we summarize the main results from our findings. We discuss these findings at more length and in the context of previous research in Section 4 before concluding in Section 5.

2 METHODS

2.1 Initial Conditions

The initial setup of the galactic disk used in this work follows closely the GALAKOS model (D’Onghia & L. Aguerri 2020), which uses a modified version of the MakeNewDisk code (Springel et al. 2005). The GALAKOS model has three components - a radially exponential and vertically isothermal stellar disk, and a stellar bulge and dark matter halo following a Hernquist profile (Hernquist 1990). All N -body runs in this work used the same setup parameters as the GALAKOS disk, more details of which can be found in the original paper.

The addition of the gas phase was done as follows. The version of MakeNewDisk used for the original GALAKOS model can generate a gas disk which is radially exponential and in vertical gravito-hydrodynamic balance. We modified the radial profile of this code in order to allow us to generate a disk with a constant surface density

within some cut-off radius, and then exponentially declining beyond that radius with the scale-length of the stellar disk. Our fiducial model used an initial surface density of $20 M_{\odot}/\text{pc}^2$ and a cut-off radius of 9.3 kpc. The initial gas disk is generated with a temperature of 10^4 K and solar metallicity.

After generating the gaseous disk in this way, we stitched the gas disk together with the GALAKOS N -body disk (and bulge and dark matter halo) after the GALAKOS disk has been allowed to evolve for 1.5 Gyr. The purpose of allowing the GALAKOS disk to evolve first for a short period of time is to allow for the bar to form unimpacted by the presence of the gas. We found that including the gas before the bar has formed disrupts the formation of the bar, as has been seen in previous work (e.g., Athanasoula et al. 2013). Throughout this work, we consider $t = 0$ for the N -body run to be the time at which we added the gas phase for the SMUGGLE run (i.e., we ignore the first 1.5 Gyr of evolution of the N -body disk when the bar is forming).

We made one additional modification when stitching the gas disk together with the N -body disk - we created a hole within the central 4 kpc. This hole guards against an initial dramatic infall of gas within the bar region, which we found to destroy the bar. It is not uncommon for observed barred galaxies to have gas deficits in the bar region (though not in the very center; Sellwood & Wilkinson 1993). Therefore, our practice of allowing the gas distribution to have a hole in the central region is consistent with our choice to begin the simulations with a bar already formed.

We used a mass resolution of $7.5 \times 10^3 M_{\odot}$ for the baryonic components (initial stellar disk, stellar bulge, and gas) and a mass resolution of $3.75 \times 10^4 M_{\odot}$ for the dark matter halo. This mass resolution is closest to “level 3” in the AURIGA simulations (Grand et al. 2017). This corresponds to approximately 6.4×10^6 particles in the stellar disk, 1.1×10^6 in the bulge, 1.2×10^6 in the gas disk, and 25.3×10^6 in the dark matter halo. We used a softening length of 0.02 kpc for all components. Snapshots were saved at equal intervals of 0.005 in the time units of the simulation, kpc/(km/s).

Our setup is initially out of equilibrium, but we found that after about 500 Myr, the system has settled into a steady-state configuration and initial transients appear not to affect the results after this point. The constant surface density of the initial gas disk is important for ensuring the gas disk is dense enough in order for comparisons to real galaxies to be appropriate.

2.2 Numerical Model

We use the Stars and Multiphase Gas in GaLaxiEs (SMUGGLE) model (Marinacci et al. 2019) implemented within the moving-mesh, finite-volume hydrodynamics and gravity code AREPO (Springel 2010). The SMUGGLE model additionally includes radiative heating and cooling, star formation, and stellar feedback. Explicit gas cooling and heating of the multi-phase interstellar medium is implemented, covering temperature ranges between 10 and 10^8 K.

Star formation occurs in cells above a density threshold ($n_{\text{th}} = 100 \text{ cm}^{-3}$) with a star-formation efficiency of $\epsilon = 0.01$. Star formation converts gas cells into star particles which represent single stellar populations with a Chabrier initial mass function (Chabrier 2003). For each star particle, the deposition of energy, momentum, mass, and metals from stellar winds and supernovae is modeled. Photo-ionization and radiation pressure are modeled using an approximate treatment. A more detailed description of this model can be found in the flagship SMUGGLE paper (Marinacci et al. 2019).

We used the fiducial model parameters, except that we increased the number of effective neighbors N_{ngb} for the deposition of feedback from 64 to 512. We found that a lower value of N_{ngb} resulted in

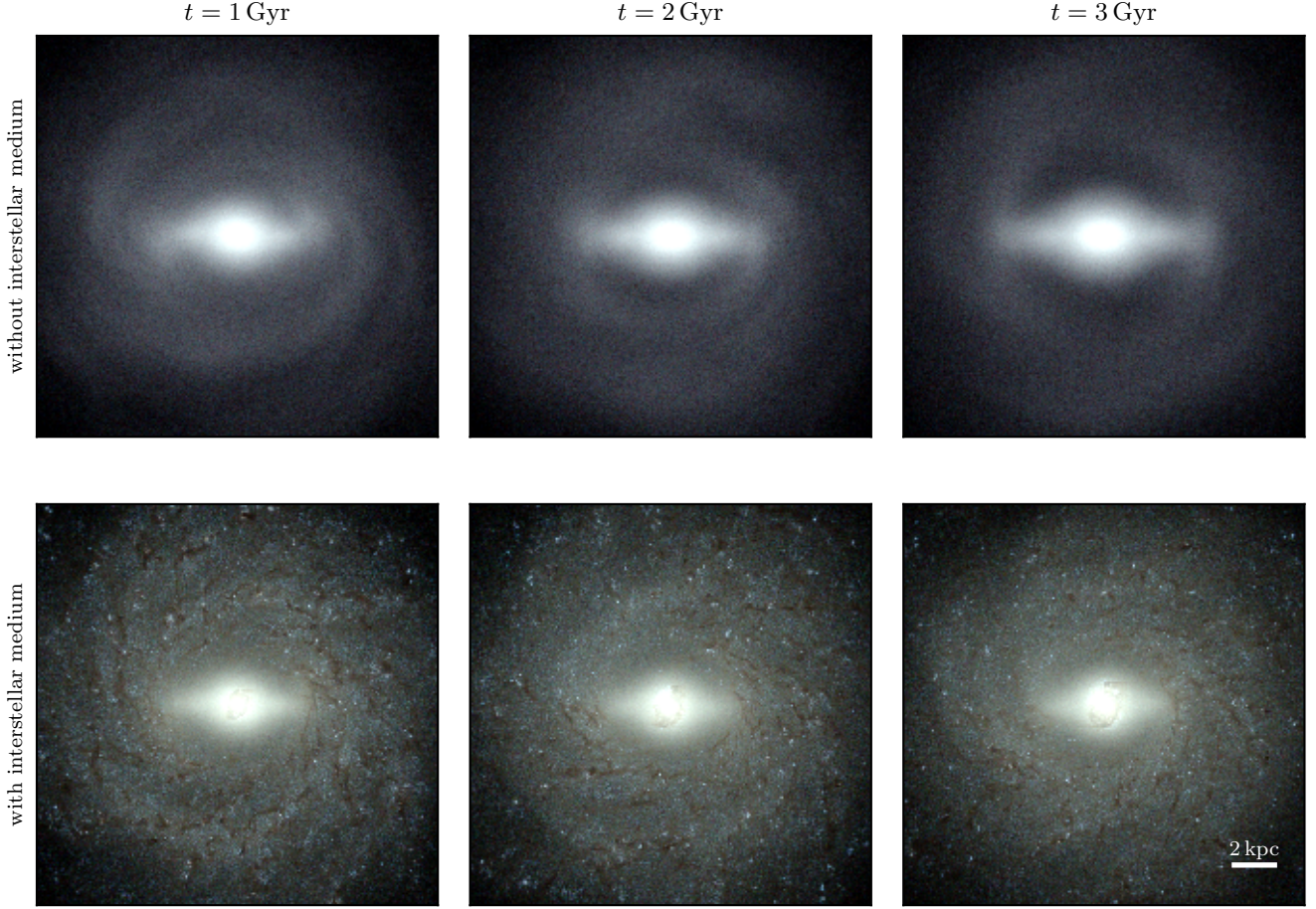


Figure 1. Synthetic Hubble Space Telescope images of our simulations with and without the interstellar medium. The upper panels show an N -body only simulation while the lower panels show a simulation which includes the SMUGGLE model for the interstellar medium. Each panel is 20 kpc to a side. Columns show different points in time, separated by 1 Gyr. We can see that in the N -body run, the bar grows in length and strength. In the SMUGGLE run, the bar remains at approximately the same length and strength over the course of the simulation. The N -body model is identical to the GALAKOS model, discussed in the text. Details on the production of these synthetic images is given in Appendix C.

inefficient photo-ionization feedback since the photo-ionizing budget had not been exhausted after deposition into 64 neighboring cells. We also used an updated version of SMUGGLE using a new mechanical feedback routine similar to the one described in Hopkins et al. (2018). This updated routine is a tensor renormalization which ensures linear and angular momentum conservation to machine precision.

In addition to the SMUGGLE model, we considered a simpler model of the interstellar medium based upon Springel & Hernquist (2003). In this model, the multiphase nature of the interstellar medium is modeled in a subgrid manner by allowing each resolution element to have a “cold” and “hot” component, with the equation of state of the gas suitably modified. Gas is allowed to interchange between the cold and hot components through processes such as cooling and stellar feedback. Cold gas is allowed to undergo star formation. We refer to this model as the smooth interstellar medium model, and it is described in more detail in Marinacci et al. (2019).

2.3 Bar Analysis

The analysis of various bar properties is performed as follows. First, the pattern speed is measured from the angle of the second Fourier component. We measured the second Fourier component by computing,

$$\begin{aligned} A_2 &= \sum_i m_i e^{i2\phi_i} \\ A_0 &= \sum_i m_i, \end{aligned} \quad (1)$$

where m_i and ϕ_i are the mass and azimuthal angle of each particle, respectively. We computed A_2 and A_0 in cylindrical bins of width 0.5 kpc from radii of 0 to 30 kpc. We defined the angle of the bar ϕ_b to be twice the angle of the complex number A_2 as measured in the bin extending from a radius of 2.5 to 3 kpc. After correcting for the periodicity of ϕ_b , we measured the pattern speed as one-half the two-sided finite gradient of ϕ_b as a function of time.

In order to compute other properties of the bar, it is necessary to decompose the disk into a barred and unbarred component. We

achieved this by following closely the methods described in [Petersen et al. \(2016\)](#). Our implementation is described in more detail in Appendix A. After the disk has been decomposed into a trapped and untrapped component, we measured the bar length as being the radius R_b which encapsulates 99% of the stars identified as being trapped in the bar.

To compute torques we used the tree algorithm in *MakeNewDisk* ([Springel et al. 2005](#)) customized to be accessible from *Python* using *Cython*. This algorithm is based on the *TREESPH* code ([Hernquist & Katz 1989](#)). We constructed a tree with an opening angle of 0.35 using only the star particles identified as being trapped in the bar. We then queried the tree at the locations of all resolution elements in the other components and computed the torque of the bar on such components. The torque on the bar by the other components is simply the negative of the torque on the other components by the bar.

2.4 Plotting Details

We saved snapshots in intervals of 0.005 in the time units of the simulation, $\text{kpc}/(\text{km/s})$, which is very nearly equal to 1 Gyr (it is ~ 0.977 Gyr). Therefore, throughout this work we referred to the native code time unit as Gyr. None of our results are sensitive to this choice.

In order to remove numerical noise in several quantities we computed, we applied a Savitzky-Golay filter ([Savitzky & Golay 1964](#)) as implemented in *scipy* using a window length of 81 and polynomial order of 3. This filter was applied to plots of pattern speeds, bar lengths and strengths, torques, and angle differences.

3 RESULTS

We show the time evolution of different bar properties in Fig. 2. In the upper panel, we show the pattern speed over time in the *N*-body (blue) and SMUGGLE (orange) runs. The pattern speed in the *N*-body case slows down while the pattern speed in the SMUGGLE case remains roughly constant. The slowing down of the pattern speed in the *N*-body case is consistent with a long line of numerical research on bars in *N*-body simulations ([Hernquist & Weinberg 1992](#); [Debattista & Sellwood 2000](#); [Athanasoula & Misiriotis 2002](#); [Athanasoula 2002, 2003](#); [O'Neill & Dubinski 2003](#); [Holley-Bockelmann et al. 2005](#); [Martinez-Valpuesta et al. 2006](#); [Weinberg & Katz 2007](#); [Dubinski et al. 2009](#)).

However, in the SMUGGLE case the pattern speed remains constant. After the first Gyr of evolution, we find that the pattern speed increases by only $\sim 10\%$ over the next 4 Gyr, compared to a $\sim 43\%$ decrease in the pattern speed for the *N*-body run over the same interval.

The bottom panel of Fig. 2 shows the torque exerted on the bar by different components. The solid lines indicate the torque on the bar by the dark matter halo, whereas the dashed line indicates the torque on the bar by the gas phase. In the *N*-body case, the halo exerts a steady negative torque on the bar, with an average torque from 1 to 4 Gyr of -58.0 in units of $10^{10} M_\odot (\text{km/s})^2$. The halo in the SMUGGLE case exerts a similar negative torque on the bar in the first Gyr of evolution, but after that the halo exerts a much smaller torque on the bar, averaging only -7.8 in the same units and over the same time interval. The gas in the SMUGGLE case exerts a steady positive torque averaging 11.7 over 1 Gyr in the same units.

As we saw qualitatively in Fig. 1, the middle panel of Fig. 3 shows that the length of the bar in the *N*-body case grows over time while it

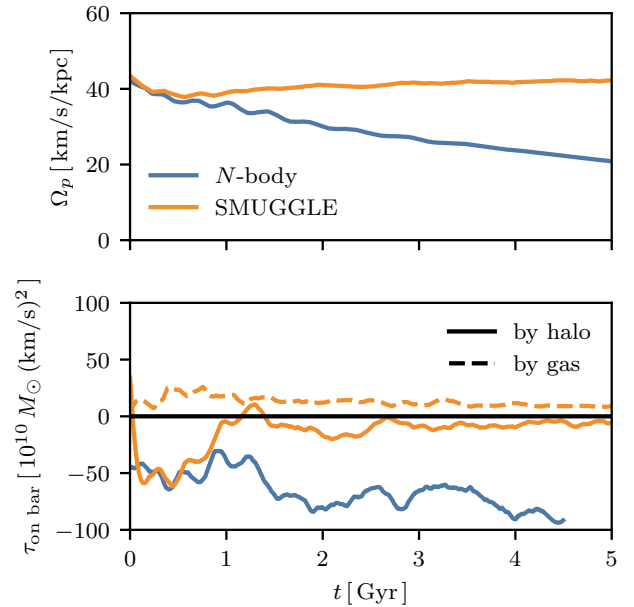


Figure 2. The upper panel shows the evolution of the pattern speed. As expected, the bar in the *N*-body run slows down due to interactions between the bar and the dark matter halo. However, the bar in the SMUGGLE run does not slow down and instead remains at a constant pattern speed. The lower panel shows the torque on the bar by different components. The solid lines show the torque exerted by the halo in both the *N*-body and SMUGGLE cases. The dashed line shows the torque exerted by the gas phase in the SMUGGLE run (there is no gas in the *N*-body run). Details on how these properties are calculated is given in the Methods section.

remains roughly constant in the SMUGGLE case. This is also consistent with previous numerical work, which found that bars tend to grow as they slow down and the radius of corotation increases ([Debattista & Sellwood 2000](#); [Athanasoula 2003](#)). The time evolution of the bar strength, defined as the maximum of $|A_2/A_0|$ as a function of radius, is shown in the lower panel Fig. 3. The quantity $|A_2/A_0|$ varies from 0 to 1, with larger values indicating a stronger bar pattern. We see that in the *N*-body case, $|A_2/A_0|$ increases over time as the bar pattern slows. This is consistent with previous *N*-body simulations which showed a clear correlation between the bar pattern speed and the bar strength (e.g., [Athanasoula 2003](#)). In the SMUGGLE case, we see that the bar strength has an initial drop but then remains at a roughly constant, but slightly decreasing, strength. This is consistent with the pattern speed in the SMUGGLE case being roughly constant or slightly increasing.

4 DISCUSSION

4.1 Pattern Speed Evolution

The lack of evolution in the pattern speed of the SMUGGLE case (seen in Fig. 2) is intimately tied to the sudden decrease in torque exerted on the bar by the dark matter halo. We argue that this can be understood in terms of the halo wake mechanism. In the *N*-body case, halo material which is resonant with the bar will form a wake which lags behind and exerts a negative torque on the bar, slowing it down ([Tremaine & Weinberg 1984a](#); [Weinberg 1985](#); [Hernquist](#)

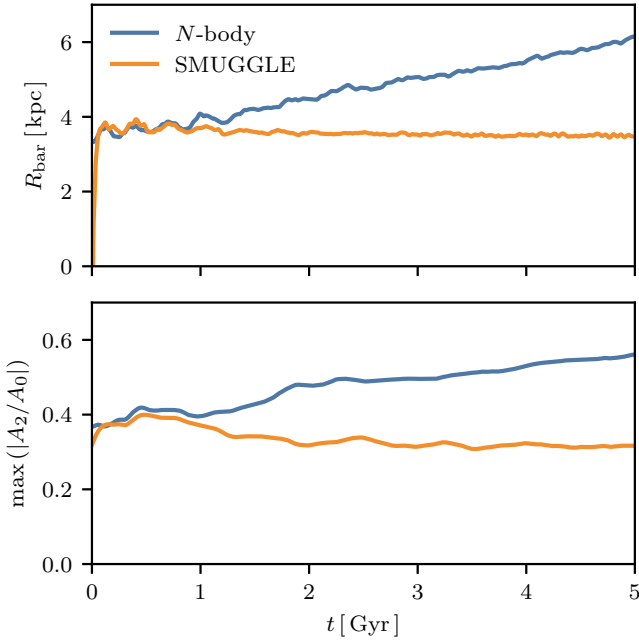


Figure 3. The evolution in bar length and strength. The *upper panel* shows the evolution of the bar length. In the N -body case, the bar lengthens. This occurs because as the pattern speed drops, bar-like orbits at larger radii are possible. Stars are captured on these orbits, lengthening the bar. This process does not occur in the SMUGGLE cases since the bar pattern speed is not decreasing, and therefore the bar length remains constant. The bar strength, shown in the *lower panel* is measured as the maximum of the second Fourier component divided by the zeroth Fourier component. We see that in the N -body case (blue) the bar strength increases with time, consistent with previous results showing that the bar strength increases as bars slow down. In the SMUGGLE case (orange), we see that the bar strength remains roughly constant, possibly slightly decreasing with time. This is also consistent with the expected relation between pattern speed and strength since the bar in this case is not slowing down.

& Weinberg 1992).² As the bar slows down, the location of the resonances in phase space changes, allowing halo material newly resonant with the bar to participate in forming the wake. However, the gas is a reliable source of positive torque on the bar, speeding the bar up. This stops the resonance location from changing such that the halo cannot reinforce the wake, arresting the process by which the halo can slow the bar down. We term this process “exhaustion.”

We can test this interpretation by measuring the angle offset between the halo wake and the bar. If the wake and the bar are aligned (i.e., there is no angle offset), then the wake cannot exert a negative torque on the bar. This angle is plotted in the left panel of Fig. 4, which shows that the angle offset is larger in the N -body case than in the SMUGGLE case by about a factor of two. The center and right panels of Fig. 4 show the halo wake with respect to the location of the bar in the N -body (center) and SMUGGLE (right) cases at one point in time.

² Since the bar is not a solid body, it is not guaranteed that a negative torque will slow it down - e.g. a negative torque could shred the bar, reducing its moment of inertia without changing its pattern speed. However, the bar seems to empirically respond to a negative torque induced by a halo wake by slowing down.

The presence of the gas can arrest the process by which additional material in the dark matter halo can contribute to a wake. However, this does not explain why the pattern speed in the SMUGGLE case is nearly constant over several Gyr. Naively, it would be a coincidence that the bar pattern speed remains constant in the SMUGGLE case, resulting from a chance cancellation of the halo and gas torques. However, a constant pattern speed in the presence of gas has been observed in a few simulations of barred galaxies with gas (Friedli & Benz 1993; Villa-Vargas et al. 2010; Athanassoula 2014). Previous work has argued this is due to the bar torquing gas inwards, but no explanation has been given for why it might remain constant.

We propose that an equilibrium mechanism is responsible for the pattern speed remaining approximately constant. In this scenario, residual negative torque from the dark matter halo balances out the positive torque from the gas phase. It has been shown when an analytic bar is forced to rotate at a constant pattern speed for a few Gyr, the halo exerts almost no torque on the bar (Chiba & Schönrich 2022). We saw in Fig. 2 that the dark matter halo in our simulation is still able to support some negative torque over a several Gyr time span.

We argue that the following occurs. First, the bar is not able to slow down quickly enough due to the positive torque of the infalling gas. This causes the resonant halo phase space at a particular pattern speed, $\Omega_{p,0}$, to become exhausted and no longer able to support a negative torque. Second, the gas is still exerting a positive torque on the bar, and therefore the pattern speed will again increase. Since at higher pattern speeds the halo has not yet been totally exhausted, the halo will once again be able to exert a negative torque on the bar. The pattern speed will then settle at a new value slightly higher than $\Omega_{p,0}$ where the gas and halo torques cancel. Over time, the pattern speed should slowly increase as the halo becomes progressively exhausted.

4.2 Delayed Gas Injection

A clear prediction of our proposed mechanism is that the constant pattern speed a particular galaxy will end up is somewhat arbitrary. In the real universe for an isolated galaxy it would be the formation pattern speed of the bar while in our simulation it is the pattern speed of the bar when gas is added to the system. We tested this by adding gas to the system at a later time when the bar has further grown and slowed down with time. In our particular test, we added the gas at a time when the pattern speed is ~ 30 km/s/kpc. As shown in Fig. 5, we find that the pattern speed evolution is very similar between the two cases (orange and red lines). If anything, the system with a lower pattern speed seems to speed up more, which is consistent with our picture since the stronger bar should experience a larger torque from the gas as it is more efficient at driving gas inflows. We also show in the Appendix B that more slowly rotating bars at fixed bar strength are more efficient at driving gas inflows as well. Nonetheless, when the initial pattern speed is lower (red line), the addition of gas does not cause the pattern speed to quickly return to the higher value of our fiducial simulation (orange line).

4.3 Varying Initial Gas Fractions

We also performed a test in which we varied the initial gas fraction of the disk. In our fiducial run, we set the surface density of the gas disk from 4 kpc to ~ 9.3 kpc to be $20 M_{\odot}/\text{pc}^2$. We also ran with surface densities of 15, 10, and $5 M_{\odot}/\text{pc}^2$. These correspond to initial gas fractions of approximately 16%, 10%, 7%, and 4%. The pattern speed evolution is shown in Fig. 6 We find that the bar in disks with initial

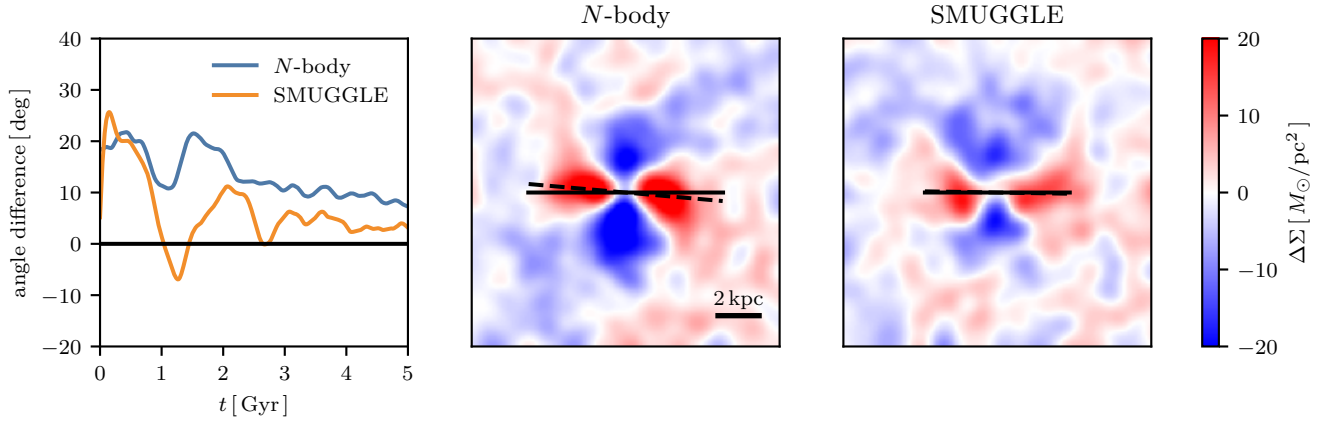


Figure 4. The wake excited in the dark matter halo. The dark matter halo wake is shown in the *N*-body case (*middle panel*) and SMUGGLE case (*right panel*) after 2.6 Gyr of evolution. The *middle* and *right panels* show a surface density projection in the *x-y* plane of the dark matter halo after an axisymmetric average has been subtracted. The solid line indicates the direction of the bar while the dashed line indicates the direction of the halo wake (both measured by taking the second Fourier component within a sphere of all material within a radius of 4 kpc). The *left panel* shows the time evolution of the angle difference between the bar and the halo wake, as measured from the second Fourier component. After the first Gyr, the angle difference in the SMUGGLE case is smaller than in the *N*-body case by about a factor of two, reflecting how the dark matter halo in the SMUGGLE case is unable to exert as negative a torque on the bar as in the *N*-body case.

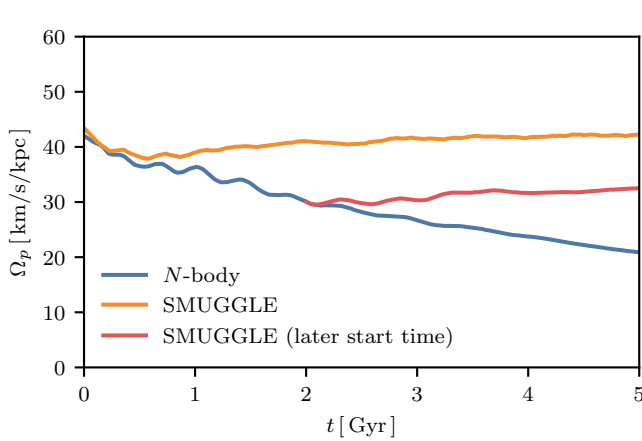


Figure 5. Pattern speed evolution with a lower initial pattern speed. We tested the evolution of our system when gas is added to the *N*-body run at a later time, but with all other simulation parameters kept the same. The setup is therefore identical to our previous runs just with a bar that is larger, stronger, and with a lower pattern speed. We find that the pattern speed evolution is very similar to our fiducial case, except that the bar retains its original pattern speed. This indicates a mechanism which keeps the bar at its formation pattern speed, and that there is not a particular pattern speed which the system tends to.

surface densities of 20, 15, and $10 M_{\odot}/\text{pc}^2$ evolve with a constant pattern speed while the bar in a disk with initial surface density of $5 M_{\odot}/\text{pc}^2$ slows down at a similar rate to the *N*-body case.

As a result, we conclude that for the disk, bar, and halo properties considered in this work, a gas fraction of only approximately 5% is necessary in order for the proposed stabilizing mechanism to operate.

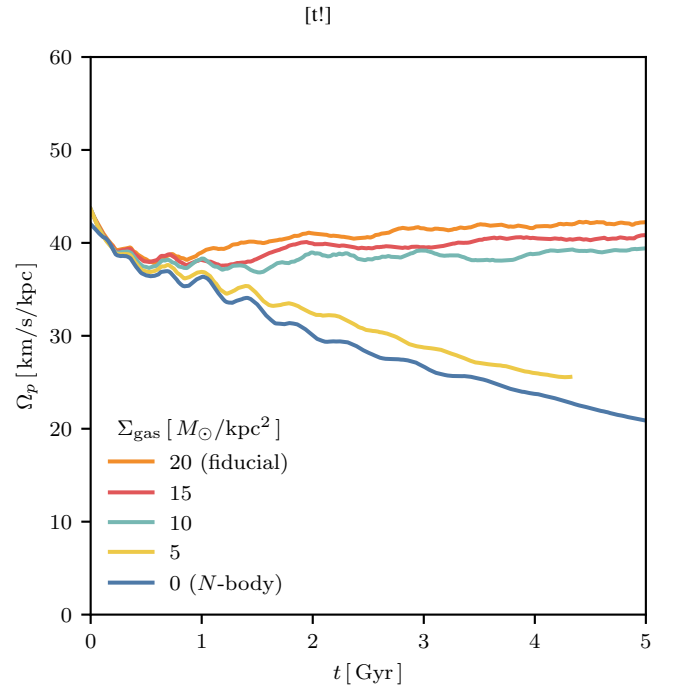


Figure 6. Pattern speed evolution with varying gas fractions. We explored the impact of lowering the initial gas surface density of our fiducial disk on the evolution of the pattern speed. The surface densities we tested of 20, 15, 10, and $5 M_{\odot}/\text{kpc}^2$ correspond to initial gas fractions of 16%, 10%, 7%, and 4%. We find that initial surface densities 20, 15, and $10 M_{\odot}/\text{kpc}^2$ result in bars which remain at a constant pattern speed, while an initial surface density of $5 M_{\odot}/\text{kpc}^2$ results in a bar which slows down in roughly the same manner as the *N*-body case.

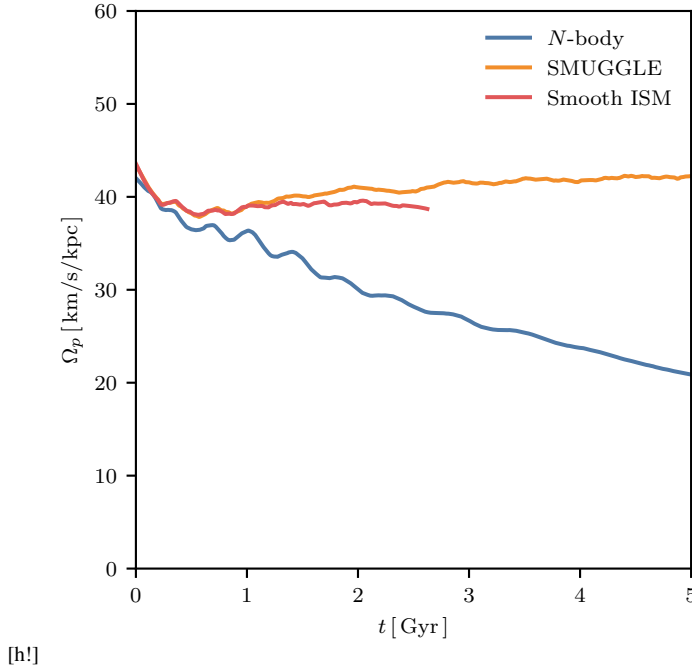


Figure 7. Pattern speed evolution of a smooth ISM model. This evolution is shown for the fiducial disk in the N -body (blue), SMUGGLE (orange), and smooth ISM (red) cases. The smooth ISM model is an older model for the ISM which treats its multiphase nature in a subgrid fashion (Springel & Hernquist 2003). This fundamentally differs from the SMUGGLE model, which explicitly resolves the hot and cold phases of the ISM (Marinacci et al. 2019). The pattern speed in the smooth ISM case is broadly similar to the evolution in the SMUGGLE case. This shows that the stability of the pattern speed is not simply a result of our assumed model for the ISM.

4.4 Smooth Interstellar Medium

We also performed a simulation of the same disk but with a simpler model of the interstellar medium (Springel & Hernquist 2003), closer to standard methods used in cosmological simulations of galaxy formation. We find that the pattern speed evolution is nearly the same in this case, and so conclude that our result is not sensitive to the details of the model for the interstellar medium. Details on the physics of this test is given in Section. X.

4.5 Observations

We note that ref. Garma-Oehmichen et al. (2020) found that the rotation parameter \mathcal{R} positively correlates with gas fraction, such that galaxies with higher gas fractions are rotating more slowly. However, it is not obvious this is in tension with our result since the gas fraction of galaxies correlates with other galactic properties Blanton & Moustakas (2009). Furthermore, the measurement of pattern speeds is a delicate process still prone to large error bars.

4.6 Cosmological Simulations

Barred galaxies in cosmological simulations of galaxy formation continue to be in conflict with observations by producing bars which rotate too slowly Algorry et al. (2017); Peschken & Lokas (2019); Fragkoudi et al. (2021). However, the pattern speeds of bars in both

cosmological simulations and the real universe can be affected by environmental processes not included in our simulation – e.g., satellite infall Purcell et al. (2011), non-sphericity Athanassoula et al. (2013) or rotation Saha & Naab (2013); Long et al. (2014); Collier et al. (2018, 2019) in the dark matter halo, or perhaps even the gaseous circumgalactic medium. Naturally, extending our present work to account for such effects is a crucial next step in understanding the formation and evolution of galactic bars.

5 CONCLUSIONS

The implications of our findings are numerous. First, we naturally explain why nearly all observed galaxies are fast rotators without requiring the inner regions of dark matter halos to be underdense Debattista & Sellwood (1998, 2000) or requiring new physics Roshan et al. (2021a,b). Second, we show that the role of gas is of paramount importance in studies which attempt to uncover the nature of dark matter from its effect of slowing down the bar Chiba et al. (2021); Chiba & Schönrich (2021). Third, we provide an explanation for how the Milky Way’s bar could be both long-lived and a fast rotator, of which there is some observational evidence Bovy et al. (2019). And finally, we complicate the picture of radial mixing expected to sculpt the Milky Way’s disk Bird et al. (2012); Hayden et al. (2015), a process which relies upon the pattern speed of the bar to change with time (though our work does not alter expectations for radial mixing induced by spiral arms Sellwood & Binney (2002)).

We found that below a certain gas fraction, bars should still be able to slow down. Therefore, we expect barred spiral galaxies which have been gas-poor for extended periods of time to be rotating very slowly. We therefore predict that observations which target such galaxies (e.g., lenticular barred galaxies Blanton & Moustakas (2009)) would find slowly rotating bars. There does exist one example of a galaxy which is known to be a slow rotator – the low surface brightness galaxy UGC 628 Chemin & Hernandez (2009). This galaxy has been studied in detail by ref. Chequers et al. (2016), who note that it indeed has a low gas fraction for galaxies of its type. We predict a general trend that bars in gas-rich spiral galaxies should rotate quickly while bars in gas-poor spiral galaxies should rotate slowly.

ACKNOWLEDGEMENTS

We would like to thank Greg L. Bryan, Neal J. Evans, Drummond B. Fielding, Keith Hawkins, Jason A. S. Hunt, Sarah M. R. Jeffreson, Kathryn V. Johnston, Peter M. W. Kalberla, Jürgen Kerp, Julio F. Navarro, Joshua S. Speagle, Martin D. Weinberg, and Yanfei Zou for helpful discussions. A.B. would like to thank Todd Phillips for helpful discussions. Some computations in this paper were run on the FASRC Cannon cluster supported by the FAS Division of Science Research Computing Group at Harvard University. Resources supporting this work were also provided by the NASA High-End Computing (HEC) Program through the NASA Advanced Supercomputing (NAS) Division at Ames Research Center. This research has made use of the Spanish Virtual Observatory (<https://svo.cab.inta-csic.es>) project funded by MCIN/AEI/10.13039/501100011033/ through grant PID2020-112949GB-I00. A.B. was supported by the Future Investigator in NASA Earth and Space Science and Technology (FINESST) award number 80NSSC20K1536 during the completion of this work. E.D. was partially supported by HST grants HST-AR-16363.001 and HST-AR-16602.006-A and by NASA Award NASA

80NSSC22K0761. J.Q. acknowledges support from NSF grant AST-2008490. L.V.S. is grateful for financial support from NASA ATP 80NSSC20K0566, NSF AST 1817233 and NSF CAREER 1945310 grants. P.T. acknowledges support from NSF grant AST-1909933, AST-2008490, and NASA ATP Grant 80NSSC20K0502. M.V. acknowledges support through NASA ATP 19-ATP19-0019, 19-ATP19-0020, 19-ATP19-0167, and NSF grants AST-1814053, AST-1814259, AST-1909831, AST-2007355 and AST-2107724.

DATA AVAILABILITY

The inclusion of a Data Availability Statement is a requirement for articles published in MNRAS. Data Availability Statements provide a standardised format for readers to understand the availability of data underlying the research results described in the article. The statement may refer to original data generated in the course of the study or to third-party data analysed in the article. The statement should describe and provide means of access, where possible, by linking to the data or providing the required accession numbers for the relevant databases or DOIs.

REFERENCES

- Aguerre J. A. L., et al., 2015, *A&A*, **576**, A102
- Algorry D. G., et al., 2017, *MNRAS*, **469**, 1054
- Athanassoula E., 2002, *ApJ*, **569**, L83
- Athanassoula E., 2003, *MNRAS*, **341**, 1179
- Athanassoula E., 2014, *MNRAS*, **438**, L81
- Athanassoula E., Misiriotis A., 2002, *MNRAS*, **330**, 35
- Athanassoula E., Machado R. E. G., Rodionov S. A., 2013, *MNRAS*, **429**, 1949
- Bird J. C., Kazantzidis S., Weinberg D. H., 2012, *MNRAS*, **420**, 913
- Blanton M. R., Moustakas J., 2009, *ARA&A*, **47**, 159
- Blitz L., Spergel D. N., 1991, *ApJ*, **379**, 631
- Bovy J., Leung H. W., Hunt J. A. S., Mackereth J. T., García-Hernández D. A., Roman-Lopes A., 2019, *MNRAS*, **490**, 4740
- Bruzual G., Charlot S., 2003, *MNRAS*, **344**, 1000
- Camps P., Baes M., 2020, *Astronomy and Computing*, **31**, 100381
- Chabrier G., 2003, *PASP*, **115**, 763
- Chemin L., Hernandez O., 2009, *A&A*, **499**, L25
- Chequers M. H., Spekkens K., Widrow L. M., Gilhuly C., 2016, *MNRAS*, **463**, 1751
- Chiba R., Schönrich R., 2021, *MNRAS*, **505**, 2412
- Chiba R., Schönrich R., 2022, *MNRAS*, **513**, 768
- Chiba R., Friske J. K. S., Schönrich R., 2021, *MNRAS*, **500**, 4710
- Collier A., Shlosman I., Heller C., 2018, *MNRAS*, **476**, 1331
- Collier A., Shlosman I., Heller C., 2019, *MNRAS*, **488**, 5788
- Contopoulos G., 1980, *A&A*, **81**, 198
- Corsini E. M., 2011, *Memorie della Societa Astronomica Italiana Supplementi*, **18**, 23
- D’Onghia E., L. Aguerri J. A., 2020, *ApJ*, **890**, 117
- Debattista V. P., Sellwood J. A., 1998, *ApJ*, **493**, L5
- Debattista V. P., Sellwood J. A., 2000, *ApJ*, **543**, 704
- Dubinski J., Berentzen I., Shlosman I., 2009, *ApJ*, **697**, 293
- Eilers A.-C., Hogg D. W., Rix H.-W., Ness M. K., 2019, *ApJ*, **871**, 120
- Eskridge P. B., et al., 2000, *AJ*, **119**, 536
- Evans N. J., Kim J.-G., Ostriker E. C., 2022, *ApJ*, **929**, L18
- Fragkoudi F., Grand R. J. J., Pakmor R., Springel V., White S. D. M., Marinacci F., Gomez F. A., Navarro J. F., 2021, *A&A*, **650**, L16
- Friedli D., Benz W., 1993, *A&A*, **268**, 65
- Garma-Oehmichen L., Cano-Díaz M., Hernández-Toledo H., Aquino-Ortiz E., Valenzuela O., Aguerri J. A. L., Sánchez S. F., Merrifield M., 2020, *MNRAS*, **491**, 3655
- Grand R. J. J., et al., 2017, *MNRAS*, **467**, 179
- Guo R., Mao S., Athanassoula E., Li H., Ge J., Long R. J., Merrifield M., Masters K., 2019, *MNRAS*, **482**, 1733
- Hayden M. R., et al., 2015, *ApJ*, **808**, 132
- Hernquist L., 1990, *ApJ*, **356**, 359
- Hernquist L., Katz N., 1989, *ApJS*, **70**, 419
- Hernquist L., Weinberg M. D., 1992, *ApJ*, **400**, 80
- Hohl F., 1971, *ApJ*, **168**, 343
- Hohl F., 1976, *AJ*, **81**, 30
- Holley-Bockelmann K., Weinberg M., Katz N., 2005, *MNRAS*, **363**, 991
- Hopkins P. F., Quataert E., 2011, *MNRAS*, **415**, 1027
- Hopkins P. F., et al., 2018, *MNRAS*, **480**, 800
- Johnson H. M., 1957, *AJ*, **62**, 19
- Jones A. P., Köhler M., Ysard N., Bocchio M., Verstraete L., 2017, *A&A*, **602**, A46
- Kalberla P. M. W., Dedes L., 2008, *A&A*, **487**, 951
- Long S., Shlosman I., Heller C., 2014, *ApJ*, **783**, L18
- Lupton R., Blanton M. R., Fekete G., Hogg D. W., O’Mullane W., Szalay A., Wherry N., 2004, *PASP*, **116**, 133
- Lynden-Bell D., Kalnajs A. J., 1972, *MNRAS*, **157**, 1
- Marinacci F., Sales L. V., Vogelsberger M., Torrey P., Springel V., 2019, *MNRAS*, **489**, 4233
- Martínez-Valpuesta I., Shlosman I., Heller C., 2006, *ApJ*, **637**, 214
- Menéndez-Delmestre K., Sheth K., Schinnerer E., Jarrett T. H., Scoville N. Z., 2007, *ApJ*, **657**, 790
- Miville-Deschênes M.-A., Murray N., Lee E. J., 2017, *ApJ*, **834**, 57
- O’Neill J. K., Dubinski J., 2003, *MNRAS*, **346**, 251
- Ostriker J. P., Peebles P. J. E., 1973, *ApJ*, **186**, 467
- Peschken N., Lokas E. L., 2019, *MNRAS*, **483**, 2721
- Petersen M. S., Weinberg M. D., Katz N., 2016, *MNRAS*, **463**, 1952
- Purcell C. W., Bullock J. S., Tollerud E. J., Rocha M., Chakrabarti S., 2011, *Nature*, **477**, 301
- Rodrigo C., Solano E., 2020, in XIV.0 Scientific Meeting (virtual) of the Spanish Astronomical Society. p. 182
- Rodrigo C., Solano E., Bayo A., 2012, SVO Filter Profile Service Version 1.0, IVOA Working Draft 15 October 2012, doi:10.5479/ADS/bib/2012ivoa.rept.1015R
- Roshan M., Banik I., Ghafourian N., Thies I., Famaey B., Asencio E., Kroupa P., 2021a, *MNRAS*, **503**, 2833
- Roshan M., Ghafourian N., Kashfi T., Banik I., Haslbauer M., Cuomo V., Famaey B., Kroupa P., 2021b, *MNRAS*, **508**, 926
- Saha K., Naab T., 2013, *MNRAS*, **434**, 1287
- Savitzky A., Golay M. J. E., 1964, *Analytical Chemistry*, **36**, 1627
- Sellwood J. A., Binney J. J., 2002, *MNRAS*, **336**, 785
- Sellwood J. A., Wilkinson A., 1993, *Reports on Progress in Physics*, **56**, 173
- Springel V., 2010, *MNRAS*, **401**, 791
- Springel V., Hernquist L., 2003, *MNRAS*, **339**, 289
- Springel V., Di Matteo T., Hernquist L., 2005, *MNRAS*, **361**, 776
- Tremaine S., Weinberg M. D., 1984a, *MNRAS*, **209**, 729
- Tremaine S., Weinberg M. D., 1984b, *ApJ*, **282**, L5
- Vasiliev E., 2019, *MNRAS*, **482**, 1525
- Villa-Vargas J., Shlosman I., Heller C., 2010, *ApJ*, **719**, 1470
- Weinberg M. D., 1985, *MNRAS*, **213**, 451
- Weinberg M. D., Katz N., 2007, *MNRAS*, **375**, 460

APPENDIX A: BAR DECOMPOSITION

Computing the length of the bar and the torque on the bar by different components requires us to decompose the disk into a component which is trapped by the bar and a component which is untrapped. In order to do this, we follow closely the technique developed in Petersen et al. (2016). We analyzed the orbit of each star particle (meaning initial disk, bulge, and newly formed stars) by extracting the x - y positions of the apoapse of each in a frame corotating with the bar, where apoapses are defined as local maxima in r . For each apoapse, we searched for the 19 closest apoapses in time and applied a k -means clustering algorithm on this set of 20 points with $k = 2$.

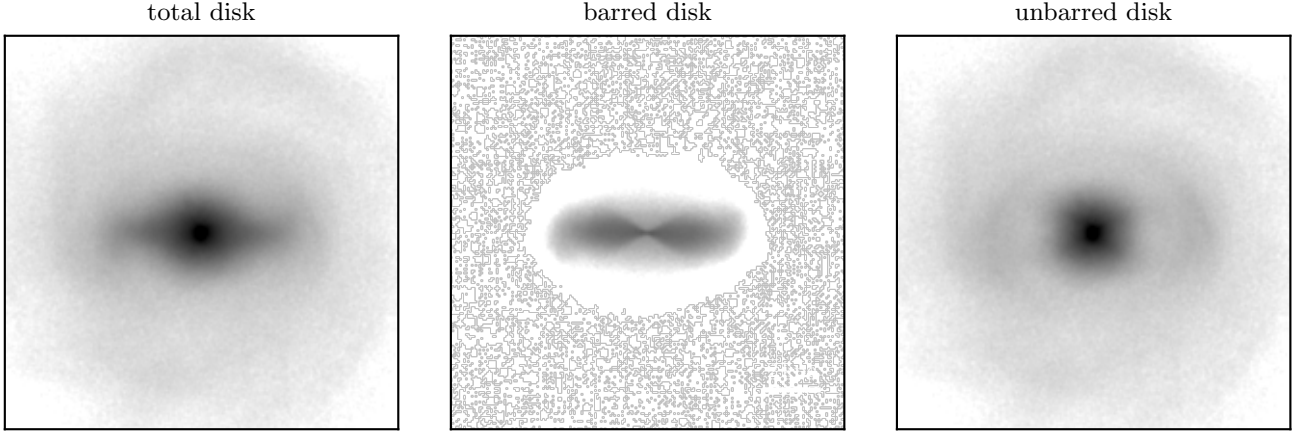


Figure A1. Disk decomposition into the barred and unbarred disk. This procedure is based on Petersen et al. (2016). The *left panel* shows a face-on surface density projection through the stellar component of the SMUGGLE simulation (disk and bulge) at $t = 1$ Gyr. The *middle panel* shows the component of the disk identified as being trapped in the bar while the *right panel* shows the component of the disk identified as not being trapped in the bar. The fact that the untrapped stars form a roughly axisymmetric structure indicates our bar decomposition is sufficiently accurate.

We then computed for each of the two clusters the average angle from the bar $\langle \Delta\phi \rangle_{0,1}$, the standard deviation in R of the points $\sigma_{R0,1}$, and the average radius of the cluster $\langle R \rangle_{0,1}$. At each apoapse, a particle was considered to be in the bar if it met the following criteria:

$$\max(\langle \Delta\phi \rangle_{0,1}) < \pi/8 \quad (\text{A1})$$

$$\frac{\sigma_{R0} + \sigma_{R1}}{\langle R \rangle_0 + \langle R \rangle_1} < 0.22 \quad (\text{A2})$$

These criterion are slightly different and simplified from the ones used in Petersen et al. (2016), but we found them to empirically work well at decomposing the disk into a bar and disk component. In Fig. A1, we show an example of this decomposition. The *left panel* shows a surface density projection of the stellar disk and bulge (including newly formed stars) from the SMUGGLE model after 1 Gyr of evolution in a frame such that the bar is aligned with the x -axis. The *middle panel* shows a projection of the subset of stars that are identified as being trapped in the bar and the *right panel* shows a projection of the stars that are not identified as being trapped. The fact that the *right panel* is roughly axisymmetric indicates the bar decomposition is performing adequately.

APPENDIX B: VARYING PATTERN SPEED

When the bar slows down, we argue that this induces a larger positive torque from the gas phase. Only gas within corotation will flow inwards, while gas outside corotation will flow outwards (Hopkins & Quataert 2011). Since the corotation radius is larger for more slowly rotating bars, it follows that more slowly rotating bars should be more efficient at driving gas inflows and thus experience a larger positive torque from the gas phase.

We performed an experiment to test this hypothesis by forcing the stellar disk in the SMUGGLE run to rotate at a constant angular rate and measuring the torque on the bar by the gas phase at different rotation rates. The result of this experiment is illustrated in Fig. B1, which shows that a more slowly rotating bar experiences a larger positive torque from the gas.

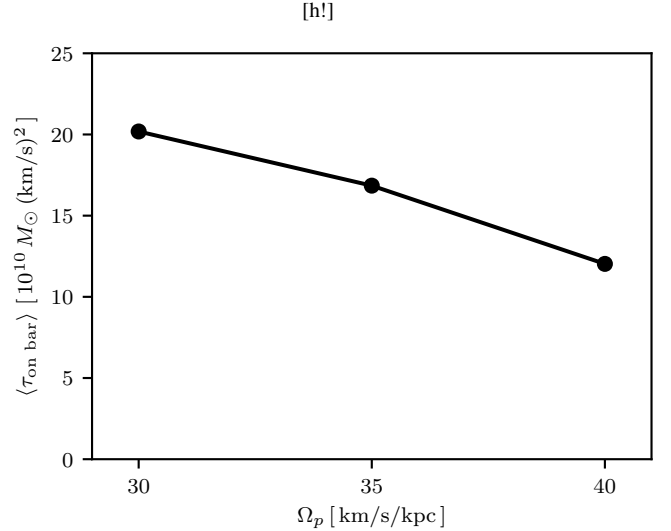


Figure B1. Average torque exerted by gas on a bar which rotates at a fixed pattern speed. Since only gas within the corotation radius is able to infall and slower bars have larger corotation radii, slower bars experience a larger net torque than faster bars. The setup of the simulations used here is identical to the SMUGGLE case discussed earlier, except the N -body disk is rotated as a solid body with a constant angular velocity.

APPENDIX C: IDEALIZED MOCK LIGHT IMAGES

We created synthetic mock light images at 1024^2 resolution in Fig. 1 for the *Hubble Space Telescope* using a post-processed Monte Carlo radiation transfer simulation with the SKIRT9 code including secondary emission from dust (Camps & Baes 2020). Emission from star particles was calculated assuming a Bruzual-Charlot spectral energy distribution (Bruzual & Charlot 2003) and a Chabrier initial stellar mass function (Chabrier 2003). The luminosity from each star particle was smoothed using a cubic spline kernel with each star particle being assigned a smoothing length equal to its distance to its 32nd closest neighbor. We launched 10^9 photon packets per sim-

ulation segment. For star particles which were present in the initial simulation (i.e., initial disk and bulge particles), we assumed that they have an age of 5 Gyr and solar metallicity. For star particles in the SMUGGLE simulation which are newly formed, we used their recorded ages and metallicities.

For the SMUGGLE simulations, we included absorption and emission from dust. We assumed the THEMIS (The Heterogeneous dust Evolution Model for Interstellar Solids) dust model (Jones et al. 2017) to convert gas metallicity and mass density to dust mass density. For the N -body simulations we ran the SKIRT9 code in a mode without an obscuring medium, but otherwise applied the same procedure.

We used the profiles for filters F814W, F606W, and F475W on the Advanced Camera for Surveys (ACS) instrument for red, green, and blue pixel values, respectively. Filtered fluxes were converted to RGB values using an arcsinh scaling following Lupton et al. (2004). Scalings and cutoff values were adjusted manually to create visually appealing images. Filter profiles were provided by the Spanish Virtual Observatory Filter Service (Rodrigo et al. 2012; Rodrigo & Solano 2020).

APPENDIX D: COMPARISON TO THE MILKY WAY

For several Gyr, our fiducial disk exhibits several properties in reasonable agreement to the Milky Way. This is uncommon in models of galaxies that include the gas phase of the disk but no circumgalactic medium. As mentioned earlier, the pattern speed seems to match the observed pattern speed of the Milky Way’s bar (Bovy et al. 2019). We briefly summarize some of the other ways our disk is comparable to the Milky Way.

We computed the circular velocity curve of our model using the AGAMA package Vasiliev (2019). We fit the baryonic component (stellar disk, bulge, gas, and newly formed stars) with an axisymmetric cylindrical spline with 20 grid points in both the radial and vertical direction spanning 0.2 to 50 kpc in the radial direction and from 0.02 to 10 kpc in the vertical direction. We fit the dark matter halo using a spherically symmetric multipole fit with a maximum angular harmonic coefficient of $l = 2$. We plot the circular velocity curve in Fig. D2 compared to observational estimates Eilers et al. (2019). The SMUGGLE disk (which includes additional mass in the form of gas) has a slightly higher circular velocity than the N -body disk which, itself, is slightly higher than the observational estimates. Overall, though, the circular velocity curves between our model and that observed in the Milky Way are broadly consistent.

We also show the evolution of the surface density profile in Fig. D1. We find that in our simulation the atomic and molecular gas surface density and the SFR surface density is broadly consistent with the expected values for the Milky Way Kalberla & Dedes (2008); Evans et al. (2022). The discrepancy between 1 and 4 kpc in the molecular and SFR surface density is likely due to the fact that the distances to molecular clouds which underlines this work used a simple kinematic distance based on an axisymmetric model of the Milky Way Miville-Deschênes et al. (2017), which is not accurate in the bar region where gas has large non-circular velocities.

This paper has been typeset from a \LaTeX file prepared by the author.

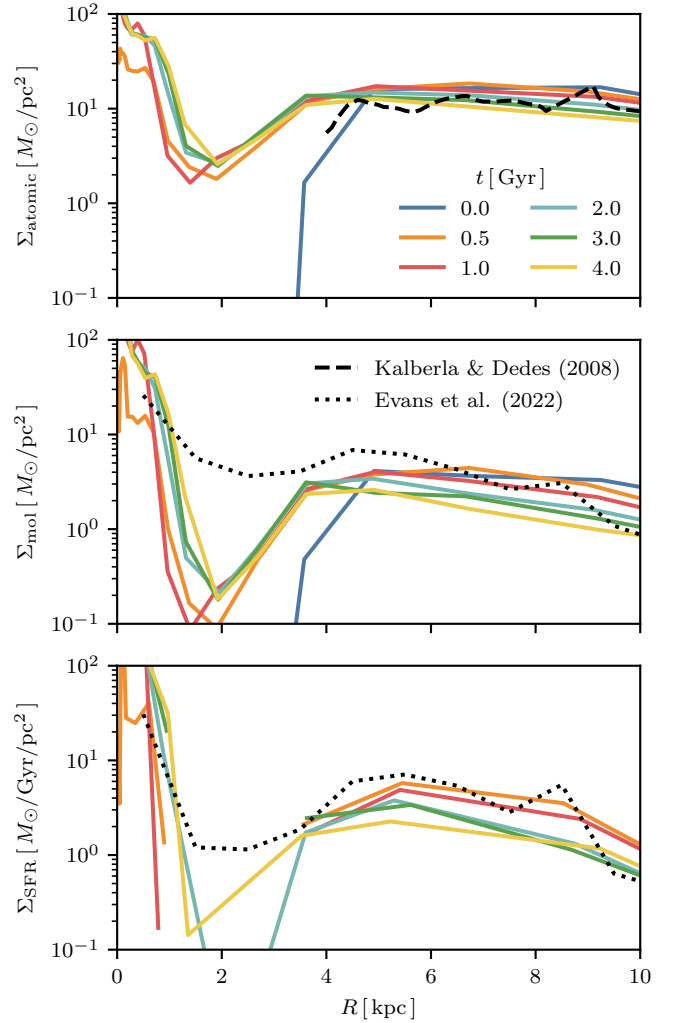


Figure D1. The time evolution of the atomic gas surface density (*upper*), molecular gas surface density (*middle*) and the star formation rate (SFR) surface density (*lower*) at various times during our fiducial simulation. Colored lines indicate the profiles at selected times during the simulation while the black dashed lines indicate observations for the atomic gas (Kalberla & Dedes 2008) and black dotted lines indicate a model which allows the CO-to-H₂ conversion factor X_{CO} to vary with metallicity (Evans et al. 2022). Molecular gas surface densities were provided separately (N. Evans, private communication). We see that the molecular gas and SFR surface densities are within an order of magnitude of the Milky Way’s typical values at all times. We see a sharp decrease in the gas and SFR surface densities along the extent of the bar from ~ 1 to ~ 4 kpc, related to the gas inflow in this region.

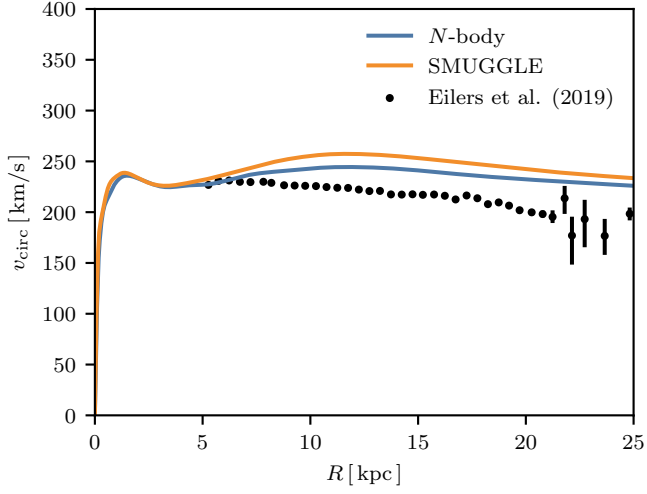


Figure D2. The circular velocity curve of our initial setups. This curve is shown for the N -body run (blue) and the SMUGGLE run (orange) compared to observational estimates for the Milky Way (Eilers et al. 2019). We see that the circular velocity curve for both runs is marginally larger than the Milky Way’s, but still comparable. The SMUGGLE circular velocity curve is larger than the N -body curve due to the additional mass in the gas phase.